Research in Astronomy and Astrophysics, 25:075001 (10pp), 2025 July

https://doi.org/10.1088/1674-4527/add670
CSTR: 32081.14.RAA.add670

Bar-driven Gas Dynamics in NGC 1097: Insights from Hydrodynamical Simulations and CO(2–1) Observations

Jie Liu[1,2], Zhi Li[3], and Juntai Shen[4,5]
[1] Shanghai Astronomical Observatory, Chinese Academy of Sciences, Shanghai 200030, China
[2] School of Astronomy and Space Sciences, University of Chinese Academy of Sciences, Beijing 100049, China
[3] Shanghai Key Lab for Astrophysics, Shanghai Normal University, Shanghai 200234, China; lizhi@shnu.edu.cn
[4] Department of Astronomy, School of Physics and Astronomy, Shanghai Jiao Tong University, Shanghai 200240, China
[5] State Key Laboratory of Dark Matter Physics, School of Physics and Astronomy, Shanghai Jiao Tong University, Shanghai 200240, China
Received 2025 April 21; accepted 2025 May 6; published 2025 June 10

Abstract

To address the disk-halo degeneracy problem, we investigate the nearby barred spiral galaxy NGC 1097. We construct mass models using 3.6 and 4.5 μm near-infrared photometric images from the S^{4}G survey, constrained by rotation curves derived from CO($J = 2$–1) data from the PHANGS-ALMA survey. These models serve as inputs for a suite of hydrodynamic simulations, where we systematically test the influence of key parameters including the disk mass scaling factor ($f_{\rm M}$), bar pattern speed ($\Omega_{\rm b}$), and gas sound speed ($c_{\rm s}$). By comparing the CO(2–1) kinematic maps in the bar region with those from the simulations, we perform a standard χ^2 analysis to identify the best-fit model. The best-fit model reproduces the observed morphological and kinematic gas features of the galaxy, indicating that NGC 1097 likely hosts a maximal disk with a slowly rotating bar. We also test the influence of a boxy/peanut-shaped (B/P) bulge by incorporating a double-peaked vertical density profile into the model. This B/P structure tends to weaken the bar's non-axisymmetric potential and necessitate a higher bar pattern speed to reproduce the observed gas morphology.

Key words: Galaxies – galaxies: kinematics and dynamics – galaxies: evolution – galaxies: fundamental parameters

1. Introduction

The flat rotation curves (RCs) observed in galaxies, extending well beyond the visible stellar disk (Roberts 1976), have long served as pivotal evidence for the presence of dark matter. While dark matter is widely accepted as the dominant component in the outer regions of galaxies, the relative contributions of baryonic and dark matter in the central regions remain uncertain. This long-standing issue, known as the disk-halo degeneracy, was clearly illustrated in van Albada et al. (1985), where they demonstrated that the RC of NGC 3198 could be reproduced equally well by models ranging from dark matter-dominated to baryon-dominated ("maximal disk") scenarios. Traditional methods have proven ineffective in breaking the degeneracy between the disk and halo mass components. Despite recent advances such as two-dimensional velocity field mapping, this degeneracy continues to significantly hinder our ability to accurately constrain the inner mass distribution of galaxies (Barnes et al. 2004).

Barred galaxies, constituting approximately 70% of disk galaxies in the near-infrared (Eskridge et al. 2000; Knapen et al. 2000; Menéndez-Delmestre et al. 2007; Barazza et al. 2008; Aguerri et al. 2009; Gadotti 2009), offer a promising avenue for breaking this degeneracy. The non-axisymmetric potential of the bar induces strong gas responses, such as shocks (visible as dust lanes) and nuclear rings, which are highly sensitive to the underlying baryonic mass distribution and bar dynamics. Hydrodynamic simulations have shown that these features can be used to constrain the bar pattern speed, mass-to-light ratio, and gas sound speed (Athanassoula 1992a, 1992b; Kim et al. 2012a, 2012b; Li et al. 2015). This methodology has been successfully applied to several galaxies, including NGC 4123 (Weiner et al. 2001a, 2001b), NGC 1365 (Lindblad et al. 1996; Zánmar Sánchez et al. 2008), ESO 566-24 (Rautiainen et al. 2004), and NGC 1291 (Fragkoudi et al. 2017), etc.

NGC 1097 is an exceptional candidate for gas dynamical modeling. This SBb-type barred spiral galaxy, located at a distance of 14.2 Mpc (Tully et al. 2009; Nasonova et al. 2011) features a prominent bar, well-defined dust lanes, and a distinct circumnuclear star-forming ring (Storchi-Bergmann et al. 2005; Fathi et al. 2006; Davies et al. 2009), making it an ideal target for studying bar-driven gas dynamics. Lin et al. (2013) employed hydrodynamic simulations to constrain the bar pattern speed and mass distribution of NGC 1097. However, several key limitations in that study motivate a re-investigation of the galaxy. First, their stellar mass model lacked constraints from near-infrared photometry, which may have led to inaccuracies in representing the stellar mass

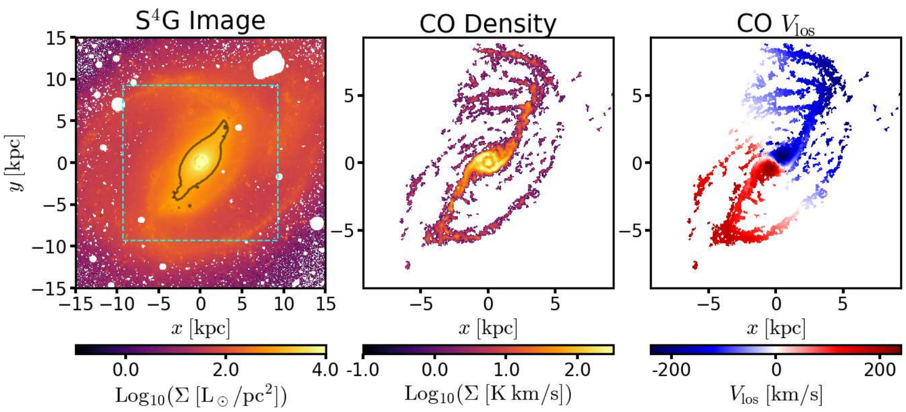

Figure 1. S^{4}G and CO(2–1) observations of NGC 1097. Left: Near-infrared (3.6 μm) surface brightness map from the S^{4}G survey showing surface brightness in units of $L_\odot$ pc^{-2} within 15 kpc. The black contours highlight the galactic bar structure, and the white regions mask foreground stars. The cyan rectangle indicates the coverage of the CO(2–1) observations shown in the subsequent panels. Middle: Integrated intensity (moment 0) map of the CO(2–1) emissions from PHANGS-ALMA, in units of K km s^{-1}, tracing the distribution of molecular gas. Right: Intensity-weighted mean velocity (moment 1) map derived from the CO(2–1) emissions, in units of km s^{-1} (white represents zero velocity).

Table 1
Properties of NGC 1097 Used in this Work

GalaxyID	Type	Bar Length ($a_{\rm bar}$)	Inclination (i)	Distance	Scale (1″)
NGC 1097	SB	6.8 kpc	46°6	14.2 Mpc	68.8 pc
Reference	Buta (2014)	this work	Salo et al. (2015)	Tully et al. (2009)	⋯

Note. The bar length ($a_{\rm bar}$) is taken as the average of measurements from the maximum isophotal ellipticity (r_ϵ) and the radius of the maximum $m = 2$ Fourier amplitude ($r_{\rm A2}$), both determined from the deprojected 3.6 μm image (see Section 5.2).

distribution. Second, the RC used to constrain their mass model was derived from older data with lower spatial and spectral resolution. Third, their exploration of the parameter space was relatively limited, and the determination of the best-fit model primarily relied on subjective visual comparison rather than quantitative criteria.

Recent advances in both observational data and simulation techniques now enable a more robust analysis. High-resolution CO(2–1) observations from the PHANGS-ALMA survey (Leroy et al. 2021) provide detailed molecular gas kinematics, while deep near-infrared imaging from the S^{4}G survey enhances stellar mass modeling accuracy. In parallel, modern simulation codes and computational resources enable large-scale, high-resolution explorations of parameter space, facilitating quantitative comparisons using statistical metrics.

In this work, we revisit NGC 1097 using updated data and refined modeling techniques. Using S^{4}G 3.6 and 4.5 μm photometry and high-quality CO RCs, we construct detailed mass models of the galaxy. We then conduct a large suite of hundreds of hydrodynamic simulations, systematically varying the disk mass scaling factor ($f_{\rm M}$), bar pattern speed ($\Omega_{\rm b}$), and gas sound speed ($c_{\rm s}$). By comparing the simulated gas response with observed morphological and kinematic features, we aim to place robust constraints on the bar dynamics and baryonic mass distribution of NGC 1097, thereby contributing to efforts to break the disk-halo degeneracy.

2. Photometric and CO(2–1) Images

The 3.6 μm photometric images from the S^{4}G survey reveal distinct structural features of NGC 1097 as shown in Figure 1. The galaxy exhibits a prominent, extended stellar bar, with an approximate length of 6.8 kpc (see Section 5.2). Despite the use of infrared wavelengths, which typically reduce the visibility of recent star formation, the circumnuclear star-forming ring remains morphologically distinct. The properties of NGC 1097 are summarized in Table 1.

The molecular gas distribution and kinematics are traced in the CO(2–1) surface brightness and line-of-sight velocity maps, shown in the middle and right panels of Figure 1, respectively. These maps are directly processed from the PHANGS-ALMA survey pipeline products. Assuming that spiral arms are trailing relative to the direction of galactic rotation (as predicted by density wave theory), observed arm geometry indicates that NGC 1097 rotates in a clockwise direction.

By combining the infrared and CO(2–1) images, we present a schematic illustration of the typical gaseous structures of barred galaxies in a face-on view (Figure 2). Prominent dust

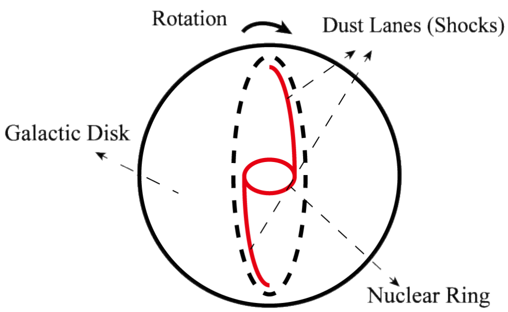

Figure 2. Schematic illustration of the typical gaseous structures in barred galaxies.

lanes are found on the leading edges of the bar, exhibiting an $m = 2$ rotational symmetry and connecting to a well-defined nuclear ring in the central region.

3. Work Procedure

3.1. Mass Model and Potential

The construction of a robust mass model is essential for understanding the dynamical evolution of barred galaxies. Our goal is to derive a gravitational potential that accurately describes the distribution of both baryonic and dark matter components.

The baryonic mass distribution is derived from 3.6 and 4.5 μm images from the S^4G survey. To account for dust contamination, we apply the empirical relation from Querejeta et al. (2015), which converts flux density (Jy) to stellar mass (solar mass):

$$\frac{M_\star}{M_\odot} = 10^{8.35} \times \left(\frac{F_{3.6}}{\mathrm{Jy}}\right)^{1.85} \times \left(\frac{F_{4.5}}{\mathrm{Jy}}\right)^{-0.85} \times \left(\frac{D}{\mathrm{Mpc}}\right)^2, \quad (1)$$

where $F_{3.6}$ and $F_{4.5}$ are the observed flux densities in Jy at 3.6 μm and 4.5 μm, respectively, and D is the distance of galaxies. A key assumption here is that the mass-to-light ratio is constant across the whole galaxy.

To minimize the impact of foreground stars, we mask prominent point sources using the mask files provided by the S^4G survey and fill the masked regions using the IRAF `imedit` task. Then we use the IRAF `ellipse` task to determine the position angles of the galactic disk ($\mathrm{PA_{disk}}$) and bar ($\mathrm{PA_{bar}}$), as well as the inclination (i). The values from our measurements are consistent with the galactic properties reported by the S^4G survey (Sheth et al. 2010).

To deproject the galaxy image to a face-on view, we assume an intrinsically circular disk and stretch the image along the observed minor axis by a factor of $\cos^{-1} i$. To obtain the three-dimensional (3D) stellar density distribution, we assume that the vertical density profile follows the isothermal-sheet model (Binney & Tremaine 2008). The final density profile is given by:

$$\rho(R, \phi, z) = \frac{1}{2z_0}\Sigma(R, \phi)\mathrm{sech}^2\left(\frac{z}{z_0}\right), \quad (2)$$

where $\Sigma(R, \phi)$ is the de-projected surface density distribution for each galaxy and z_0 is the scale height of the disk. (z_0 is constant here, see Section 5.4 for variations).

Despite masking point sources and interpolating over the masked regions, some irregularities may remain in the surface brightness map. To smooth the derived surface density map and isolate large-scale non-axisymmetric structures (primarily the bar), we apply a Fourier decomposition in azimuth to the deprojected surface density $\Sigma(R, \phi)$:

$$\Sigma(R, \phi) = \frac{a_0}{2} + \sum_{m=1}^{\infty}[a_m(R)\cos m\phi + b_m(R)\sin m\phi], \quad (3)$$

where the Fourier coefficients $a_m(R)$ and $b_m(R)$ are given by

$$a_m(R) = \frac{1}{\pi}\int_0^{2\pi} \Sigma(R, \phi)\cos m\phi \, d\phi,$$
$$b_m(R) = \frac{1}{\pi}\int_0^{2\pi} \Sigma(R, \phi)\sin m\phi \, d\phi, \quad (4)$$

This decomposition allows us to separate the galactic surface density into different m-fold rotational symmetric components. The axisymmetric disk component is represented by $m = 0$, while the bar is primarily described by the $m = 2$ component. To construct the smoothed potential for simulations, we reconstruct the surface density using only the low-order even Fourier components ($m = 0, 2, 4, 6, 8$), while discarding odd and higher-order even components.

We adopt a spherical Navarro–Frenk–White (NFW) model (Navarro et al. 1995) to describe the dark matter halo, with its density profile given by:

$$\rho_{\mathrm{NFW}}(r) = \frac{\rho_{0,\mathrm{NFW}}}{(r/r_{0,\mathrm{NFW}})(1 + r/r_{0,\mathrm{NFW}})^2}, \quad (5)$$

where $\rho_{0,\mathrm{NFW}}$ is the characteristic density and $r_{0,\mathrm{NFW}}$ is the scale radius of the NFW halo.

To construct the total mass model, we integrate both baryonic and dark matter components. We adjust the mass scaling factor of the baryonic component to match the observed stellar mass distribution, while fine-tuning the NFW parameters ($\rho_{0,\mathrm{NFW}}$ and $r_{0,\mathrm{NFW}}$) to account for the contribution of dark matter. Additionally, if required to match the central rise of the RC, we include a central mass concentration (CMC) modeled as a Plummer sphere. The density profile of the Plummer sphere is given by:

$$\rho_{\mathrm{Plum}}(r) = \rho_{0,\mathrm{Plum}}\left(1 + \frac{r^2}{r_{0,\mathrm{Plum}}^2}\right)^{-5/2}, \quad (6)$$

where $\rho_{0,\mathrm{Plum}}$ is the central density and $r_{0,\mathrm{Plum}}$ is the scale length.

With these three components, the three-dimensional total density distribution and the galaxy's total mass must satisfy the following relation:

$$\begin{cases} \rho_{\rm total}(R,\,\phi,\,z) = f_{\rm M}\,\cdot\,\rho_{\rm disk}(R,\,\phi,\,z) + \rho_{\rm NFW}(r) + \rho_{\rm Plum}(r) \\ M_{\rm total} = f_{\rm M}\,\cdot\,M_{\rm disk} + M_{\rm NFW} + M_{\rm Plum} \end{cases}, \tag{7}$$

where $f_{\rm M}$ is the free parameter controlling the mass of disk.

The free parameters (including the mass scaling factor $f_{\rm M}$ defined in Section 3.3, the NFW parameters $\rho_{0,\rm NFW}$, $r_{0,\rm NFW}$, and the Plummer parameters $\rho_{0,\rm Plum}$, $r_{0,\rm Plum}$ if used) are iteratively adjusted so that the 1D RC derived from the total mass model is broadly consistent with the observed RC in regions assumed to be dominated by circular motion. However, we do not aim to precisely fit the entire observed RC from the PHANGS-ALMA survey. Specifically, we exclude the radial range influenced by the bar (approximately between the nuclear ring radius and the bar end) from the RC fitting process, as strong non-circular motions within this region violate the assumptions of standard RC derivation methods (Liu et al. 2025).

The exclusion of RC data between the nuclear ring radius and the bar ends is a crucial aspect of our modeling strategy. This choice is motivated by the considerable uncertainties in the observed RC within this zone. The PHANGS-ALMA RCs are derived using the conventional tilted-ring method, which assumes purely circular motion—an assumption that breaks down in the presence of strong non-circular motions induced by the bar. In our previous study (Liu et al. 2025), we systematically demonstrated that such non-circular motions can introduce significant biases in RC measurements, particularly in barred galaxies. By omitting these dynamically complex regions, we ensure that our mass models are constrained by more reliable kinematic data, thereby improving the robustness of our dynamical analysis.

Our goal is to ensure that the overall mass distribution of the model, including both baryonic and dark matter components, produces a RC that is consistent with the observed RC in regions unaffected by strong non-circular motions. By focusing exclusively on areas where the assumptions of axisymmetry and circular motion hold, we enhance the reliability and interpretability of our results.

Based on the refined mass models, we compute the gravitational potential by solving the Poisson equation:

$$\nabla^2\Phi(R,\,\phi,\,z) = 4\pi G\rho(R,\,\phi,\,z). \tag{8}$$

This potential is then used to simulate the gas dynamics as described in the following sections.

3.2. Simulation Setup

The simulations are performed using the grid-based magnetohydrodynamic (MHD) code Athena++ (Stone et al. 2020) on a uniform Cartesian grid. The adopted spatial resolution exceeds that of the S^4G photometric images (∼50 pc). The computational domain is a two-dimensional square spanning 36 kpc × 36 kpc, with coordinate boundaries of $|x| \leqslant 18$ kpc and $|y| \leqslant 18$ kpc. The grid comprises 2048 × 2048 cells, yielding a cell size of 17.6 pc, which is approximately one-third of the observational spatial resolution.

The simulations begin with an axisymmetric gravitational potential and a gaseous disk with circular rotation in centrifugal force equilibrium. Subsequently, we transform this axisymmetric potential into a non-axisymmetric one with its strength increasing linearly until it reaches its maximum over one bar evolution period ($2\pi/\Omega_b$). Our tests confirm that while this transformation timescale influences the rate at which the gas flow patterns develop, it does not affect their final morphology or detailed characteristics.

Table 2
Model Parameters for NGC 1097

$f_{\rm M}$	$\rho_{0,\rm NFW}$ ($M_\odot$ kpc^{-3})	$r_{0,\rm NFW}$ (kpc)	$\rho_{0,\rm Plum}$ ($M_\odot$ kpc^{-3})	$r_{0,\rm Plum}$ (kpc)
0.6	4.0×10^7	10	7.0×10^{10}	0.35
0.7	2.4×10^7	12	6.5×10^{10}	0.35
0.8	1.4×10^7	15	5.7×10^{10}	0.35
0.9	8.0×10^6	20	5.2×10^{10}	0.35
1.0	9.0×10^6	15	4.5×10^{10}	0.35
1.1	5.0×10^6	20	4.0×10^{10}	0.35
1.2	3.0×10^6	20	3.5×10^{10}	0.35
1.25	2.0×10^6	20	3.25×10^{10}	0.35
1.3	1.0×10^6	25	3.0×10^{10}	0.35
1.35	5.0×10^5	25	2.75×10^{10}	0.35
1.4	0	30	2.5×10^{10}	0.35

3.3. Free Parameters

In this study, we focus on three key parameters:

1. *Mass scaling factor*. ($f_{\rm M}$) scales the contribution of the stellar component (derived from the S^4G images) to the total gravitational potential. Detailed parameter settings for different $f_{\rm M}$ models are provided in Table 2.
2. *Isothermal sound speed*. ($c_{\rm s}$[km s^{-1}]) represents the velocity dispersion or turbulence level of gas.
3. *Bar pattern speed*. (Ω_b[km s^{-1} kpc^{-1}]) determines the rotational speed of the galactic bar.

For NGC 1097, we consider four values for the isothermal sound speed: 10, 15, 20 and 25 km s^{-1}. The pattern speed is varied in the range of 11–46 km s^{-1} kpc^{-1}, and the mass scaling factor ranges from 0.6 to 1.4. Notably, when $f_{\rm M} = 1.4$, the contribution required from the dark matter halo (NFW component) to match the outer RC becomes negligible. In total, 286 models have been tested. When adjusting the $f_{\rm M}$ ratio, we simultaneously change the parameters of the dark

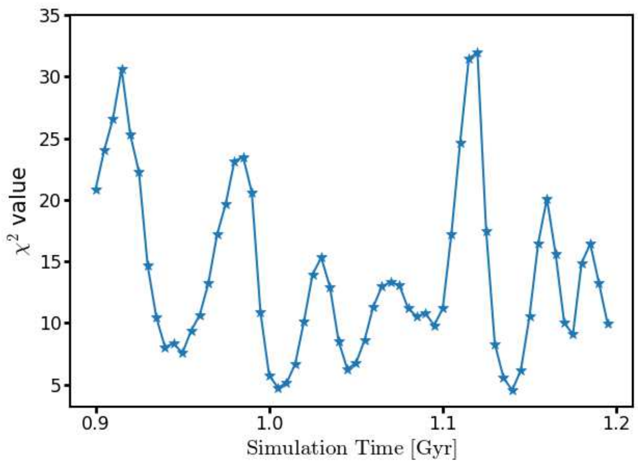

Figure 3. χ^2 evolution from $t = 0.9$ Gyr to $t = 1.2$ Gyr for $f_M = 1.0$, $c_s = 20\ \text{km s}^{-1}$, $\Omega_b = 26\ \text{km s}^{-1}\ \text{kpc}^{-1}$ model of NGC 1097.

matter halo and the Plummer sphere to ensure that the total RC remains consistent with the observed 1D RC.

3.4. Best-fit Model Determination

To identify the best-fit models in a systematic manner, we employ the standard χ^2 method to evaluate the goodness-of-fit between the models and observations for the velocity fields.

The standard χ^2 comparison is defined as:

$$\chi^2 = \frac{1}{n}\sum_n \left(\frac{V_{\text{model,los}}(x_n, y_n) - V_{\text{data,los}}(x_n, y_n)}{\sigma_{\text{los}}(x_n, y_n) + 12\ \text{km s}^{-1}}\right)^2, \quad (9)$$

where σ_{los} is the uncertainty in the observed line-of-sight velocity, and n is the number of selected pixels.

To address the singularity problem caused by pixels with extremely small uncertainties dominating the χ^2 calculation, we empirically add $12\ \text{km s}^{-1}$ to the uncertainties. This regularization ensures that the modified χ^2 provides a reliable estimate of the similarity.

Although the gas flow patten remains relatively stable, the substructures on pc-scale fluctuate along time. This dynamism is reflected in the distinct χ^2 values obtained from different time snapshots for one simulation (Figure 3). These variations are driven by short-timescale processes that reshape the gas micro-structure, with wiggle instability playing a key role (Kim et al. 2014). Wiggle instability arises from the generation of potential vorticity at deformed shock fronts, disrupting dust lanes and forming small clumps of gas with high vorticity. These clumps rapidly travel along the dust lanes from the outer regions toward the galactic center. The periodic oscillations in χ^2 values over time—clearly visible in Figure 3—serve as a distinct hallmark of the wiggle instability.

To mitigate the disruptive effects of wiggle instability on the goodness-of-fit, we compile all simulation snapshots within a 300 Myr period after three bar evolution times. A time-averaged snapshot is then produced from these data to facilitate quantitative comparison with observations.

4. Results from Simulations

The typical gas flow pattern evolves and stabilizes as the bar grows, eventually reaching a quasi-steady state when the non-axisymmetric potential reaches its maximum. We compare the steady-state gas flow patterns from the simulations with the observed ones. Our analysis shows that as the mass scaling factor (f_M), pattern speed (Ω_b), and sound speed (c_s) increase, the nuclear ring becomes smaller, the dust lanes shift closer to the bar's major axis, and become more straight. These trends are consistent with the findings of Maciejewski (2004a, 2004b), Kim et al. (2012a, 2012b), Li et al. (2015).

Figure 4 presents the χ^2 distribution for different models, with the global minimum clearly indicating the best-fit model characterized by $f_M = 1.25$, $c_s = 25\ \text{km s}^{-1}$ and $\Omega_b = 26\ \text{km s}^{-1}\ \text{kpc}^{-1}$. Additionally, it is essential to verify that the gas flow patterns in the best-fit model, identified by the χ^2 minimum, closely resemble the observations. Figure 5 shows the best-fit model, which reproduces the primary gaseous structures including the nuclear ring, the bar-driven dust lanes, and even the upper segment of the outer spiral arms. The size and position of these features closely match the observations.

5. Discussion

5.1. Maximal Disk or Zero Disk?

In addition to the χ^2 comparisons, further direct evidence supporting models with a large mass scaling factor f_M is illustrated in Figure 6. In low-f_M models, the dust lanes exhibit noticeable deviations or misalignments compared to those observed in the CO(2–1) map, and the nuclear rings are larger than the observation.

A maximal disk is defined as contributing more than 75% of the total rotation curve at $R = 2.2\,R_d$ ($V_{\text{c,disk}}(2.2R_d)/V_{\text{c,total}}(2.2R_d) \geqslant 75\%$). For NGC 1097, the disk scale length (R_d) is $\sim$3.7 kpc, as derived from the S^4G 3.6 μm image. In the best model of NGC 1097, baryons contribute more than 85% of total RC even extending to 18 kpc. Thus, this galaxy prefers a maximal disk model.

5.2. Fast Bar or Slow Bar?

There is physical limitation on the pattern speed of Galactic bar. A galactic bar cannot rotate too fast, which can be described by the equation:

$$\mathcal{R} = \frac{R_{\text{CR}}}{a_{\text{bar}}} \geqslant 1, \quad (10)$$

where R_{CR} and a_{bar} are the co-rotation radius and the bar length, respectively. Debattista & Sellwood (2000) separate galactic bars into fast ($\mathcal{R} \leqslant 1.4$) and slow($\mathcal{R} > 1.4$) bars.

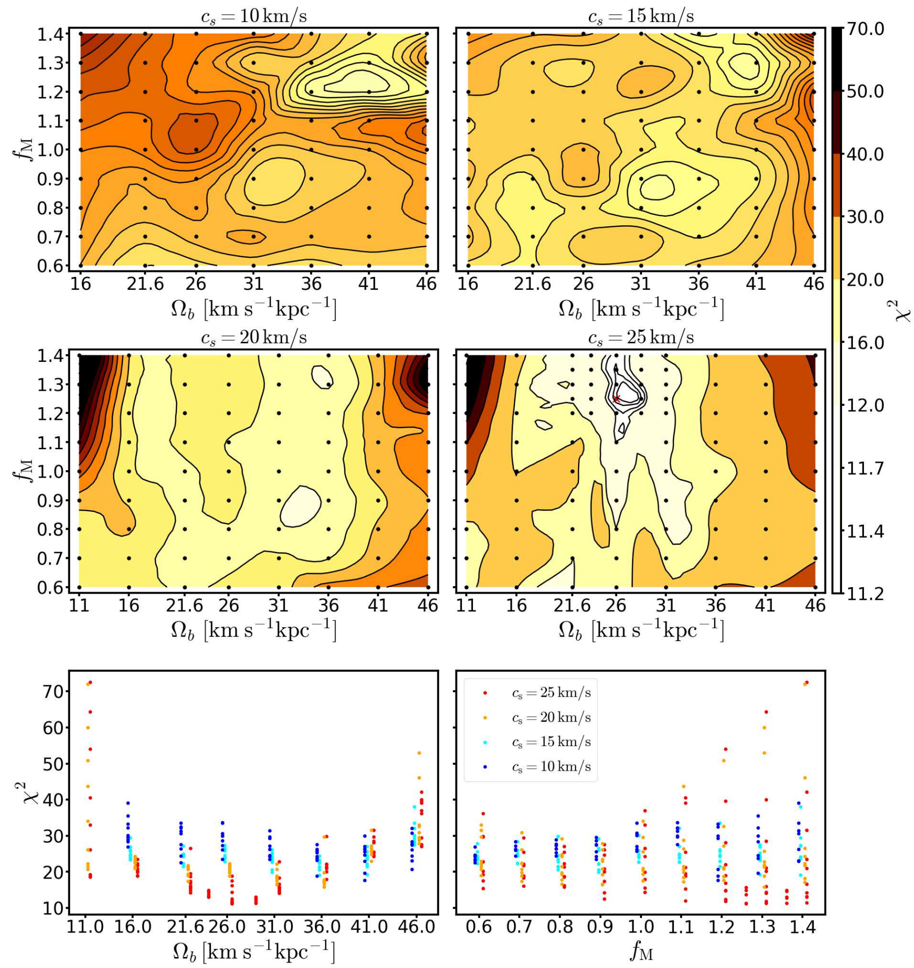

Figure 4. Distribution of χ^2 for different c_s and $f_{\rm M}$ models of NGC 1097. Upper panel: Contour plots of χ^2 for $c_s = 10$, 15, 20, 25 km s^{-1}, respectively, as a function of Ω_b (*x*-axis) and $f_{\rm M}$ (*y*-axis). Colors indicate χ^2 values, with black for higher values and white for lower values. Black contours denote specific χ^2 levels, and the red cross marks the global minimum χ^2 point. Bottom panel: Scatter plots of χ^2 as a function of Ω_b (left) and $f_{\rm M}$ (right) for different c_s. The data points are slightly offset horizontally for clarity.

The dimensionless parameter $\mathcal{R}$ can be attained from frequency diagram like Figure 7. The circular frequency $\Omega(R)$ and epicycle frequency $\kappa(R)$ are calculated from equations as follows:

$$\Omega^2(R) = \frac{1}{R}\left(\frac{\partial \Phi}{\partial R}\right),\ \kappa^2(R) = R\frac{d\Omega^2}{dR} + 4\Omega^2, \tag{11}$$

where $R = \sqrt{x^2 + y^2}$ and Φ is the potential of the galaxy.

There are several methods for measuring bar length in disk galaxies. Wozniak & Pierce (1991) proposed a widely used approach that identifies the bar length as the radius corresponding to the maximum ellipticity of isophotes, denoted as r_ϵ. However, Shen & Sellwood (2004), Athanassoula (2005) noted that this measure tends to provide a lower limit to the actual bar length.

Erwin & Sparke (2003) instead adopted the radius of the first ellipticity minimum following r_ϵ as the bar length. Athanassoula & Misiriotis (2002) introduced a Fourier decomposition approach and defined the bar length as the radius where the A_2/A_0 profile reaches its maximum, denoted as $r_{\rm A2}$. (Kataria & Shen 2022) demonstrated that r_ϵ and $r_{\rm A2}$ both underestimated the true bar length. They showed that a Fourier analysis method based on monitoring phase angle variations—with thresholds of 5° (a_5) and 10° (a_{10})—yielded a more reliable estimate of the bar length, thereby effectively addressing this systematic underestimation in an *N*-body simulation model.

Laurikainen & Salo (2002) proposed using the maximum of the Q_T (the ratio of the maximum tangential force to the averaged axisymmetric radial force) profile, as introduced by Combes & Sanders (1981), to determine the bar length.

Figure 8 provides a detailed overview of the methods used to determine the bar length of NGC 1097. For this galaxy, Fourier analysis yields threshold radii of $a_5 = 13.8$ kpc and $a_{10} = 14.0$ kpc, while the bar length from the Q_T profile is only 5.5 kpc. These values deviate significantly from the visually

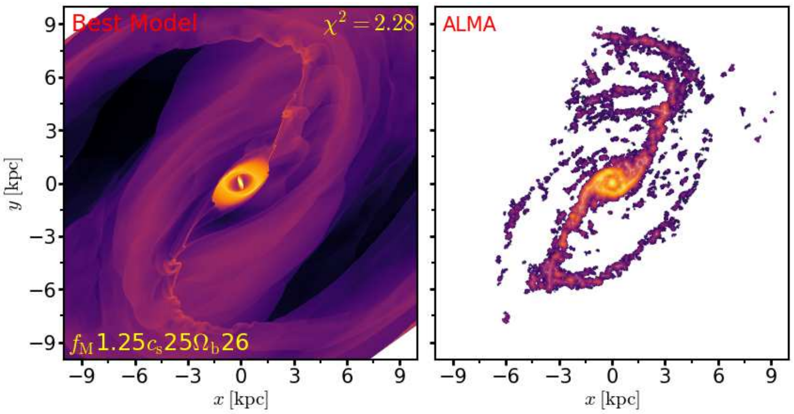

Figure 5. Comparison of the best-fit model's surface density snapshot with the observed CO(2–1) surface brightness for NGC 1097.

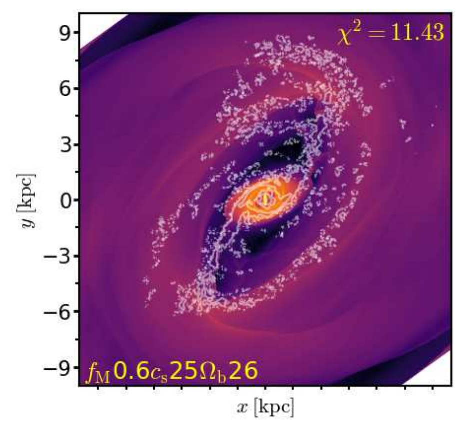

Figure 6. Surface density snapshot from the simulation with low disk mass fraction, overlaid with white contours representing the CO(2–1) surface brightness. The model parameters are: $f_{\rm M} = 0.6$, $c_{\rm s} = 25$ km s^{-1}, $\Omega_b = 26$ km s^{-1} kpc^{-1}.

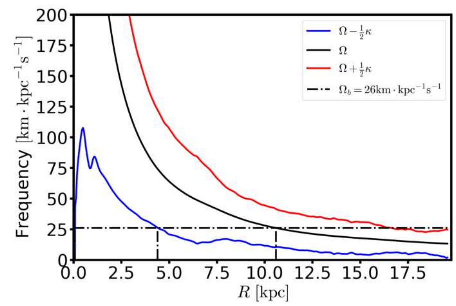

Figure 7. Frequency curves for $f_{\rm M} = 1.25$ models of NGC 1097. Blue, black, red solid lines represent $\Omega - \frac{1}{2}\kappa$, Ω, $\Omega + \frac{1}{2}\kappa$ calculated from azimuthally averaged potential. The horizontal dashed dotted line corresponds to $\Omega_b = 26$ km s^{-1} kpc^{-1}. Inner Lindblad resonance (ILR), corotation radius (CR) and outer Lindblad resonance (OLR) are outlined at points of intersections.

inferred bar length. To obtain a more reliable estimate, we adopt the average of the radius of maximum isophotal ellipticity, $r_\epsilon = 7.2$ kpc, and the peak radius of the A_2/A_0 Fourier profile, $r_{\rm A2} = 6.4$ kpc (See Table 1), resulting in a final bar length of 6.8 kpc for NGC 1097. Empirically assuming a 10% uncertainty in the bar length estimates, we derive the dimensionless parameter $\mathcal{R}$ for the best-fit model: $\mathcal{R} = 1.51^{+0.17}_{-0.14}$ (NGC 1097: $f_{\rm M}$ 1.25 $c_{\rm s}$ 25 Ω_b 26), indicating that the bar rotates at an intermediate pattern speed.

5.3. Best Models Compared with Literature

NGC 1097 is a well-studied barred galaxy, and its bar pattern speed has been investigated extensively using various methods. Lin et al. (2013) conducted numerical simulations and found a best-fit bar pattern speed of 21.6 km s^{-1} kpc^{-1}, which is slightly lower than our result. This discrepancy is likely due to the adoption of a lower observed RC in their mass model construction.

Piñol-Ferrer et al. (2014) applied orbit-based dynamical modeling to fit Hα data deriving a bar pattern speed of 36 ± 2 km s^{-1} kpc^{-1}. Font et al. (2014) employed the phase-reversal method (Font et al. 2011) to determine the corotation radius and corresponding pattern speed, yielding $38.3^{+2.3}_{-2.1}$ km s^{-1} kpc^{-1}.

In addition, the model-independent Tremaine–Weinberg (TW) method (Tremaine & Weinberg 1984) provides a direct approach to measuring a bar pattern speed. Using this method, Fathi et al. (2009) obtained 30 ± 8 km s^{-1} kpc^{-1} based on Spitzer images, while Williams et al. (2021) derived $39.9^{+2.6}_{-0.8}$ km s^{-1} kpc^{-1} using CO(2–1) data.

In summary, our derived bar pattern speed for NGC 1097 is relatively low compared to values reported in previous studies.

5.4. Boxy-peanut Scale Height Test

Boxy/Peanut-shaped bulges (B/P bulges) are commonly seen in barred spiral galaxies. Both observational and numerical studies suggest that B/P bulges originate from the buckling instability or vertical resonances after bar formation (Combes et al. 1990;

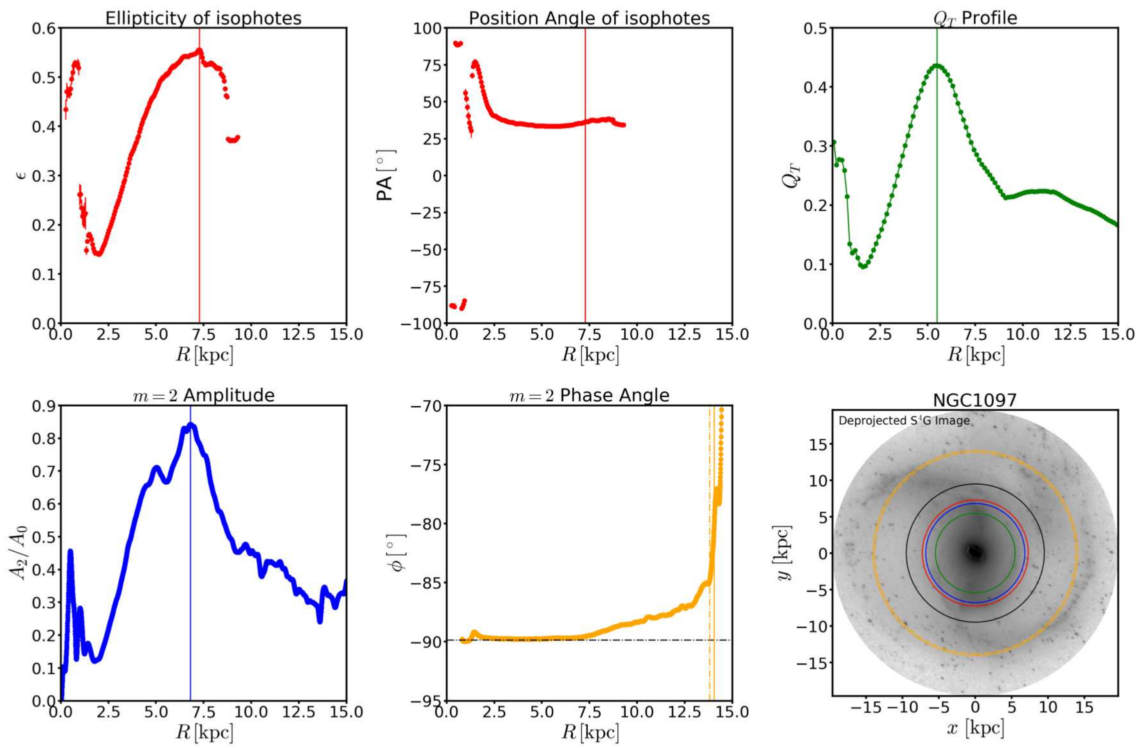

Figure 8. Bar length measurements derived using different methods. Top panel: Ellipticity (left), position angle of isophotes (middle), and Q_T profile (right). Bottom panel: $m = 2$ amplitude (left), phase angle (middle), and the deprojected S^4G image of NGC 1097 (right). The orange dashed and solid circles indicate a_5 and a_{10}, while the blue, red, and green circles correspond to r_{A2}, r_ϵ, and r_{QT}, respectively. The black circle represents the average of r_{A2}, r_ϵ, r_{QT}, a_5, and a_{10}.

Raha et al. 1991; Sellwood & Gerhard 2020). One important consequence is that the vertical scale height of the galactic disk becomes strongly radially dependent, rendering traditional constant scale height models inadequate.

To quantitatively characterize the morphology of B/P bulges, we construct a parameterized scale-height model, expressed mathematically as:

$$h_z(x, y) = A\left[\exp\left(-\left(\frac{x^2}{2\sigma^2} + \frac{(y - a_{\rm bar}/2)^2}{2\sigma^2}\right)\right) + \exp\left(-\left(\frac{x^2}{2\sigma^2} + \frac{(y + a_{\rm bar}/2)^2}{2\sigma^2}\right)\right)\right] + \begin{cases} \dfrac{h_0}{k} + \left(1 - \dfrac{1}{k}\right)h_0\dfrac{R}{a_{\rm bar}} & R \leqslant a_{\rm bar}, \\ h_0 & R > a_{\rm bar}. \end{cases} \quad (12)$$

The first term (a double Gaussian) describes the twin-peaked structure of the B/P bulge, where the amplitude A controls the peak height and σ determines the sharpness of the peaks. The second term represents the radial gradient of the central disk's scale height, with h_0 as the baseline scale height. This model is a modified version of the scale height function proposed by Fragkoudi et al. (2017).

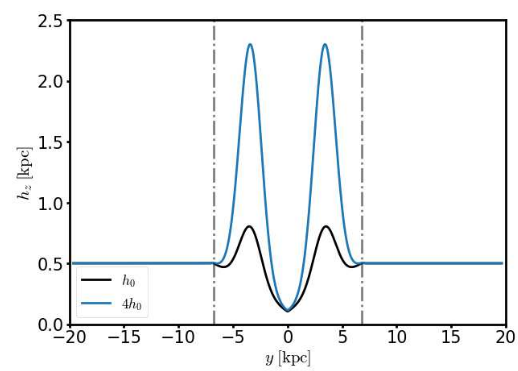

Figure 9. Side-on view of the vertical scale height distribution. The black solid line corresponds to $A = h_0 = 500$ pc, while the blue line represents a thicker B/P case with $A = 2$ kpc. Other parameters are fixed at $k = 5$, $\sigma = 1$ kpc.

The scale height can be more intuitively visualized in Figure 9. Systematic uncertainties may arise from the complex morphology of the bar (Athanassoula 2016), variations in the orientation of the B/P axis, and environmental effects such as mergers or external pressure. These factors significantly hinder precise parameter determination. Due to computational limitations, our study provides only a preliminary exploration in this direction with some qualitative insights.

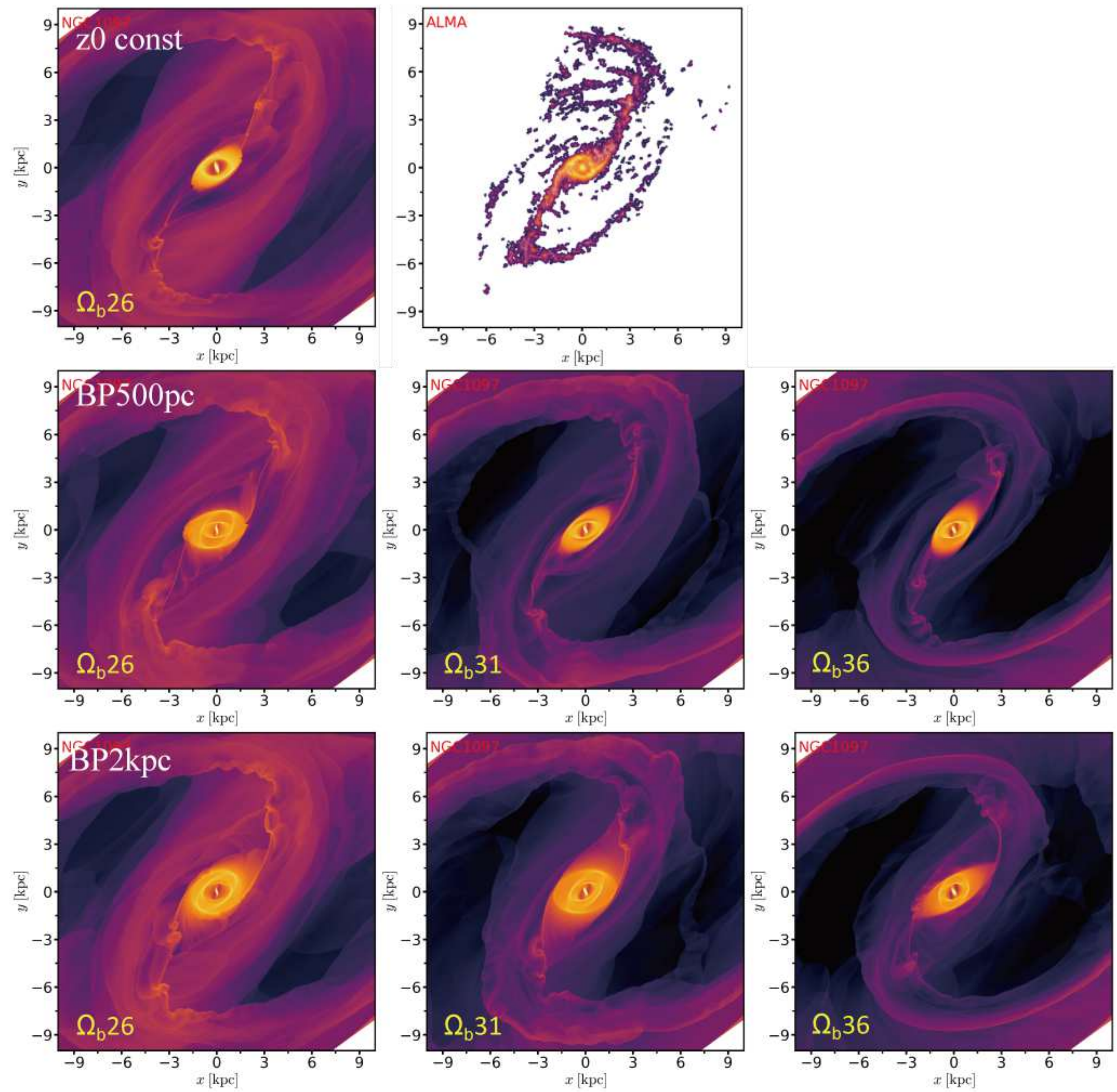

Figure 10. Effects of incorporating a vertical scale-height function to model boxy/peanut (B/P) structures on the simulated gas morphology. Top row: The original best-fit model for NGC 1097, assuming a constant scale height, alongside the corresponding CO(2–1) observational map. Middle row: Simulated gas morphologies for the weak B/P model ($A = 500$ pc) at bar pattern speeds of 25, 31, and 36 km s^{-1} kpc^{-1}. Bottom row: Results for the strong B/P model ($A = 2$ kpc) with the same pattern speed settings as the middle row.

To investigate the impact of B/P bulges on gas dynamics, we incorporate the above scale-height model into the best-fit hydrodynamical model for NGC 1097. We fixed the parameters at $k = 5$, $\sigma = 1$ kpc and test the effects of both weak (e.g., $A = 500$ pc) and strong (e.g., $A = 2$ kpc) B/P bulges. As shown in Figure 10, the twin-peaked vertical scale-height distribution weakens the non-axisymmetric gravitational potential in the bar region. Simultaneously, the reduced scale height in the central region enhances the radial gravitational force, resulting in a larger nuclear ring. Consequently, a faster bar rotation is preferred to reproduce the observed nuclear ring size and the dust lane morphology.

Our current double-peaked model involves a few parameters making it necessary to conduct statistical analyses of edge-on barred galaxies based on observations to better constrain these parameters and refine the model.

6. Summary

We investigate the gaseous structures of NGC 1097 by systematically investigating three key free parameters: the disk mass scaling factor (f_M), bar pattern speed (Ω_b), and the sound speed of the gas (c_s). The mass model is constructed based on photometric data from the S^{4}G survey, and high-resolution hydrodynamical simulations are performed. High-resolution

CO(2–1) data from the PHANGS–ALMA survey are used to constrain and evaluate the models. Our main conclusions are as follows:

1. The best-fit model ($f_{\rm M} = 1.25$) suggests that NGC 1097 hosts a maximal stellar disk, contributing 85% of $V_{\rm c,total}$ at $R = 2.2\,R_d$.
2. If assuming a constant scale-height disk, the bar in NGC 1097 rotates more slowly than typical barred galaxies ($\Omega_{\rm b} = 26$ km s^{-1} kpc^{-1}, $\mathcal{R} \sim 1.5$), placing it in the slow-rotating bar regime.
3. Scale height tests for NGC 1097 show that introducing a double-peaked vertical profile to represent the boxy/peanut-shaped (B/P) bulge structure (with peak amplitudes varying from $A = 0.5$ to 2 kpc) weakens the non-axisymmetric gravitational potential of the bar. As a result, reproducing the observed gas morphology requires an increase of the bar pattern speed in the corresponding models.

This study provides a framework for future dynamical modeling of disk galaxies. We plan to follow the approach presented in this paper to construct more dynamical modeling on other barred galaxies. Additionally, incorporating additional physical processes such as star formation and supernova feedback into our simulations, may offer deeper insights into the interplay between bar dynamics and the interstellar medium.

Acknowledgments

The research presented here is partially supported by the National Natural Science Foundation of China under grant Nos. 12103032, 12025302, 11773052 and 11761131016 (NSFC-DFG); by the "111" Project of the Ministry of Education of China under grant No. B20019; and by the China Manned Space Project under grant No. CMS-CSST-2025-A11. J.S. also acknowledges support from a Newton Advanced Fellowship awarded by the Royal Society and the Newton Fund. This work made use of the Gravity Supercomputer at the Department of Astronomy, Shanghai Jiao Tong University, and the facilities of the Center for High Performance Computing at Shanghai Astronomical Observatory.

ORCID iDs

Jie Liu https://orcid.org/0000-0003-4052-8785

References

Aguerri, J. A. L., Méndez-Abreu, J., & Corsini, E. M. 2009, A&A, 495, 491
Athanassoula, E. 1992a, MNRAS, 259, 328
Athanassoula, E. 1992b, MNRAS, 259, 345
Athanassoula, E. 2005, MNRAS, 358, 1477
Athanassoula, E. 2016, in Astrophysics and Space Science Library, Vol. 418, Galactic Bulges, ed. E. Laurikainen, R. Peletier, & D. Gadotti, (Berlin: Springer), 391
Athanassoula, E., & Misiriotis, A. 2002, MNRAS, 330, 35
Barazza, F. D., Jogee, S., & Marinova, I. 2008, ApJ, 675, 1194
Barnes, E. I., Sellwood, J. A., & Kosowsky, A. 2004, AJ, 128, 2724
Binney, J., & Tremaine, S. 2008, Galactic Dynamics: Second Edition (Princeton, NJ: Princeton Univ. Press)
Buta, R. J. 2014, in ASP Conf. Ser. 480, Structure and Dynamics of Disk Galaxies, ed. M. S. Seigar & P. Treuthardt (San Francisco, CA: ASP), 53
Combes, F., Debbasch, F., Friedli, D., & Pfenniger, D. 1990, A&A, 233, 82
Combes, F., & Sanders, R. H. 1981, A&A, 96, 164
Davies, R. I., Maciejewski, W., Hicks, E. K. S., et al. 2009, ApJ, 702, 114
Debattista, V. P., & Sellwood, J. A. 2000, ApJ, 543, 704
Erwin, P., & Sparke, L. S. 2003, ApJS, 146, 299
Eskridge, P. B., Frogel, J. A., Pogge, R. W., et al. 2000, AJ, 119, 536
Fathi, K., Beckman, J. E., Piñol-Ferrer, N., et al. 2009, ApJ, 704, 1657
Fathi, K., Storchi-Bergmann, T., Riffel, R. A., et al. 2006, ApJL, 641, L25
Font, J., Beckman, J. E., Epinat, B., et al. 2011, ApJL, 741, L14
Font, J., Beckman, J. E., Zaragoza-Cardiel, J., et al. 2014, MNRAS, 444, L85
Fragkoudi, F., Athanassoula, E., & Bosma, A. 2017, MNRAS, 466, 474
Gadotti, D. A. 2009, MNRAS, 393, 1531
Kataria, S. K., & Shen, J. 2022, ApJ, 940, 175
Kim, W.-T., Kim, Y., & Kim, J.-G. 2014, ApJ, 789, 68
Kim, W.-T., Seo, W.-Y., & Kim, Y. 2012a, ApJ, 758, 14
Kim, W.-T., Seo, W.-Y., Stone, J. M., Yoon, D., & Teuben, P. J. 2012b, ApJ, 747, 60
Knapen, J. H., Shlosman, I., & Peletier, R. F. 2000, ApJ, 529, 93
Laurikainen, E., & Salo, H. 2002, MNRAS, 337, 1118
Leroy, A. K., Schinnerer, E., Hughes, A., et al. 2021, ApJS, 257, 43
Li, Z., Shen, J., & Kim, W.-T. 2015, ApJ, 806, 150
Lin, L.-H., Wang, H.-H., Hsieh, P.-Y., et al. 2013, ApJ, 771, 8
Lindblad, P. A. B., Lindblad, P. O., & Athanassoula, E. 1996, A&A, 313, 65
Liu, J., Li, Z., & Shen, J. 2025, ApJ, 980, 146
Maciejewski, W. 2004a, MNRAS, 354, 883
Maciejewski, W. 2004b, MNRAS, 354, 892
Menéndez-Delmestre, K., Sheth, K., Schinnerer, E., Jarrett, T. H., & Scoville, N. Z. 2007, ApJ, 657, 790
Nasonova, O. G., de Freitas Pacheco, J. A., & Karachentsev, I. D. 2011, A&A, 532, A104
Navarro, J. F., Frenk, C. S., & White, S. D. M. 1995, MNRAS, 275, 720
Piñol-Ferrer, N., Fathi, K., Carignan, C., et al. 2014, MNRAS, 438, 971
Querejeta, M., Meidt, S. E., Schinnerer, E., et al. 2015, ApJS, 219, 5
Raha, N., Sellwood, J. A., James, R. A., & Kahn, F. D. 1991, Natur, 352, 411
Rautiainen, P., Salo, H., & Buta, R. 2004, MNRAS, 349, 933
Roberts, M. S. 1976, ComAp, 6, 105
Salo, H., Laurikainen, E., Laine, J., et al. 2015, ApJS, 219, 4
Sellwood, J. A., & Gerhard, O. 2020, MNRAS, 495, 3175
Shen, J., & Sellwood, J. A. 2004, ApJ, 604, 614
Sheth, K., Regan, M., Hinz, J. L., et al. 2010, PASP, 122, 1397
Stone, J. M., Tomida, K., White, C. J., & Felker, K. G. 2020, ApJS, 249, 4
Storchi-Bergmann, T., Nemmen, R. S., Spinelli, P. F., et al. 2005, ApJL, 624, L13
Tremaine, S., & Weinberg, M. D. 1984, ApJL, 282, L5
Tully, R. B., Rizzi, L., Shaya, E. J., et al. 2009, AJ, 138, 323
van Albada, T. S., Bahcall, J. N., Begeman, K., & Sancisi, R. 1985, ApJ, 295, 305
Weiner, B. J., Sellwood, J. A., & Williams, T. B. 2001a, ApJ, 546, 931
Weiner, B. J., Williams, T. B., van Gorkom, J. H., & Sellwood, J. A. 2001b, ApJ, 546, 916
Williams, T. G., Schinnerer, E., Emsellem, E., et al. 2021, AJ, 161, 185
Wozniak, H., & Pierce, M. J. 1991, A&AS, 88, 325
Zánmar Sánchez, R., Sellwood, J. A., Weiner, B. J., & Williams, T. B. 2008, ApJ, 674, 797